Interaction of caisson foundations with a seismically rupturing normal fault: centrifuge testing versus numerical simulation

M. LOLI*†, M. F. BRANSBY*, I. ANASTASOPOULOS† and G. GAZETAS†

Dramatic failures have occurred in recent earthquakes as a result of the interplay of surface structures with outcropping fault ruptures, highlighting the need to account for fault-induced loading in seismic design. Current research into the mechanisms of fault rupture–foundation–structure interaction has revealed a potentially favourable role of caissons in comparison with other foundation types. This paper explores the mechanisms of normal fault rupture interaction with rigid caisson foundations, with an integrated approach using both experiments and analysis. A series of centrifuge model tests were first conducted to study the response of a square (in plan) caisson foundation of dimensions 5 m × 5 m × 10 m, founded on a 15 m thick layer of dry dense sand. A nonlinear three-dimensional numerical simulation of the problem was then developed, and adequately validated against centrifuge test results. Depending on its position relative to the fault, the caisson interacts with the fault rupture, sometimes modifying spectacularly the free field rupture path. Acting as a kinematic constraint, the caisson 'forces' the rupture to divert on either one, or both, of its sides. The numerical study was subsequently extended to gain further insight into the effect of the exact position of the caisson relative to the fault outcrop. Different mechanisms taking place for different caisson positions are identified, and their effect on the response of the system is discussed.

KEYWORDS: centrifuge modelling; earthquakes; numerical modelling; soil/structure interaction

Les tremblements de terre survenus récemment ont donné lieu à des défaillances spectaculaires, sous l'effet de l'interaction de structures de surface avec des ruptures de failles affleurantes, en soulignant ainsi la nécessité de tenir compte des charges dues à des failles dans les études sismiques. La recherche actuelle sur les mécanismes de l'interaction entre les ruptures de failles et les fondations /structures ont révélé le rôle potentiellement favorable des fondations sur caissons par rapport à d'autres types de fondations. La présente communication se penche sur les mécanismes d'interaction normale entre des ruptures de failles et les fondations rigides sur caissons, avec une méthode intégrée à base d'expériences et d'analyses. On procède initialement à une série d'essais sur maquette centrifuge pour étudier la réaction de fondations sur caisson carré (en plan) de 5 × 5 × 10 m, placées sur une couche de sable dense et sec de 15 m d'épaisseur. On effectue ensuite une simulation numérique tridimensionnelle non linéaire du problème, que l'on valide ensuite de façon adéquate avec les résultats des essais centrifuges. En fonction de sa position relativement à la faille, le caisson interagit avec la rupture de la faille, en modifiant parfois de façon spectaculaire le chemin de rupture à champ libre. En agissant comme une contrainte cinématique, le caisson « force » la rupture à se dévier vers l'un de ses côtés, ou les deux. On renforce, par la suite, l'étude numérique afin d'acquérir des données additionnelles sur l'effet de la position exacte du caisson relativement à l'affleurement de la faille. La communication identifie différents mécanismes qui se déroulent pour différentes positions du caisson, et examine leur effet sur la réponse du système.

INTRODUCTION

Faults, although being the generation source of earthquakes, were traditionally given little attention by the engineering community. The devastating earthquakes of 1999 in Turkey and Taiwan, however, came to prove that surface fault ruptures can be a significant hazard for structures, and highlighted the need to develop design methods and guidelines against faulting-induced loading. A variety of structures were crossed by the surface fault rupture during the Kocaeli (Turkey, 1999) and Chi-Chi (Taiwan, 1999) earthquakes, and a significant number of field case histories have been reported in the literature (e.g. Chang *et al.*, 2000; Youd *et al.*, 2000; Dong *et al.*, 2003; Pamuk *et al.*, 2005; Faccioli *et al.*, 2008). Characteristic examples of failures caused by the dip-slip (normal and reverse) fault rupture during the two earthquakes are shown in Fig. 1.

Comprehensive study of field observations and associated numerical analyses (Anastasopoulos & Gazetas, 2007a, 2007b) revealed that a fascinating interplay takes place between the propagating fault rupture, the soil, the foundation and the supported structure. This was called 'fault rupture–soil–foundation–structure interaction' (FR-SFSI) by Anastasopoulos & Gazetas (2007a). The type of foundation appeared to be one of the crucial factors affecting the performance of the system during faulting events. Depending on their rigidity, continuity and surcharge loading, some foundations proved capable of effectively diverting the fault rupture and isolating the superstructure from the imposed fault deformation. This indicated that any effort to develop design recommendations against fault-induced loading should concentrate on the key role of the foundation, and study the suitability of different foundation types. Consequently, a set of practical design recommendations was proposed by Gazetas *et al.* (2008).

A significant amount of analytical (Yilmaz & Paolucci, 2007; Paolucci & Yilmaz, 2008; Anastasopoulos *et al.*, 2008, 2009) and experimental (Bransby *et al.*, 2008a, 2008b; Ahmed & Bransby, 2009) work has been conducted, focusing on the interaction of dip-slip fault ruptures with surface foundations. However, to date very little (and only numerical) research has considered the behaviour of deep founda-
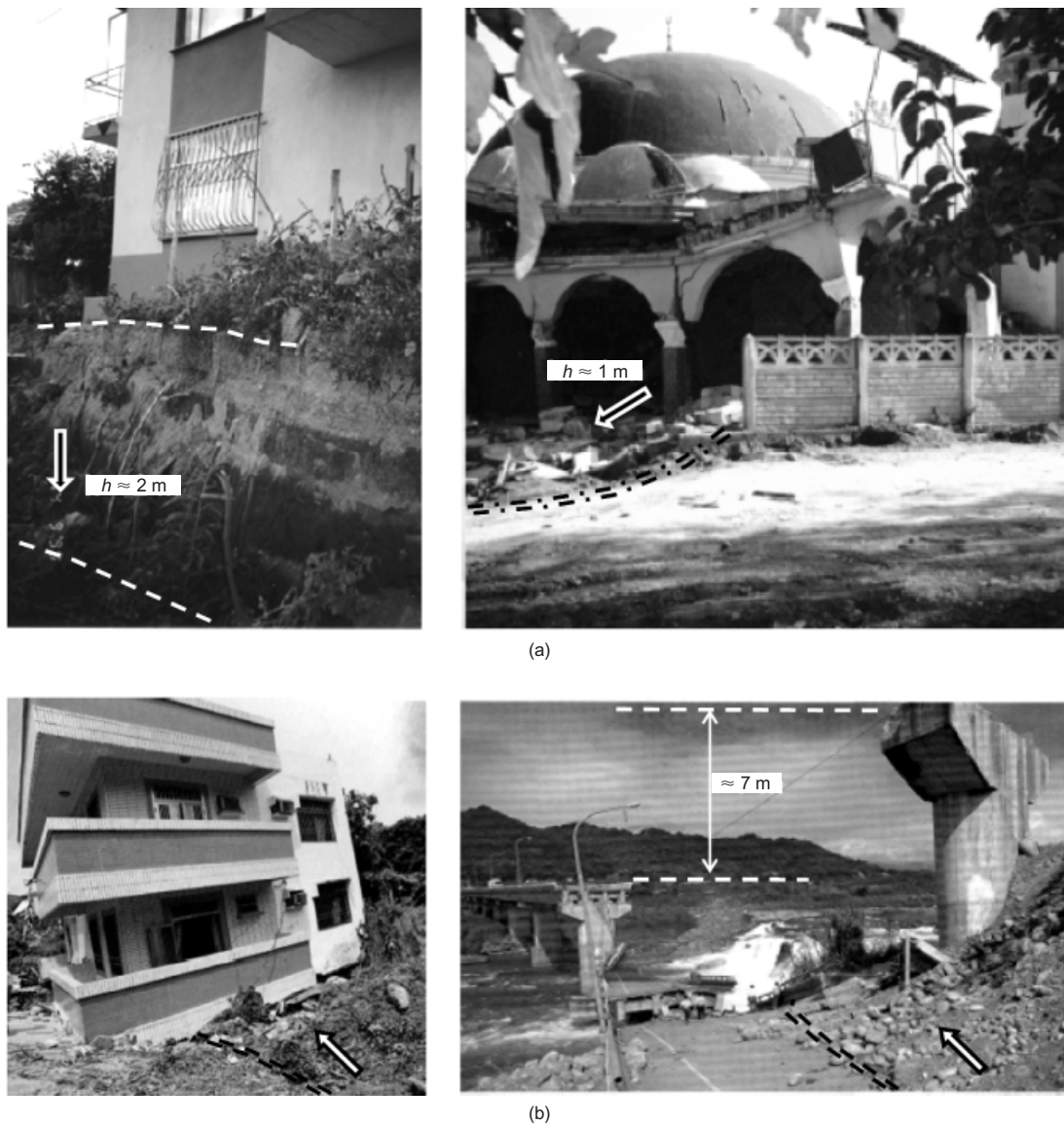
Fig. 1. Examples of fault-induced failures in recent earthquakes: (a) normal fault rupture interaction with buildings in Denizevler during 1999 Kocaeli earthquake in Turkey; (b) failures of two low-rise buildings and Bei-Fung Bridge due to thrust faulting in 1999 Chi-Chi earthquake in Taiwan

tions (Anastasopoulos *et al.*, 2008). Consequently, this study aims at investigating the interaction of rigid caisson foundations with normal fault-induced deformation and assessing their response in regard to possible design recommendations.

Deep foundations, caissons and piles, are commonly used in practice for the support of bridge piers. Because of their large length, bridges are more likely than most other structures to cross known or unknown seismically active faults, and therefore they are particularly susceptible in experiencing surface fault rupture hazards. Anastasopoulos *et al.* (2008) investigated the response of bridges supported on deep foundations (piles and caissons) subjected to local normal fault movements. This study highlighted the favourable effect of caisson foundations as opposed to piled foundations, because of the ability of the caisson foundations to divert the fault rupture (which piled foundations cannot do). This paper reports a further investigation of the problem of fault rupture–caisson interaction, aiming to gain further insight into the performance of caisson foundations subjected to tectonic deformation.

The paper reports integrated research involving both centrifuge model testing and numerical simulation. A series of centrifuge experiments were carried out to investigate the response of the caisson foundation, concentrating on the effects of its position relative to the fault rupture. After validating the effectiveness of the numerical analysis methodology against experimental results, a parametric study was conducted to offer additional insight into the effect of foundation location, and these results are discussed with respect to future bridge pier design.

PROBLEM DEFINITION AND METHODOLOGY

Figure 2 indicates schematically the main features of the problem studied, and defines the Cartesian coordinate system adopted. A $5 \, \text{m} \times 5 \, \text{m} \times 10 \, \text{m}$ square caisson foundation is considered, supported on a 15 m thick layer of dense ($D_r \approx 80\%$) dry sand. Normal fault displacement of vertical amplitude h (throw), dipping at $60°$, is applied at the bedrock. The caisson geometric characteristics were selected in such way as to represent the foundation of a typical (12 m high) highway bridge pier carrying a 1200 Mg deck (Anastasopoulos *et al.*, 2008).

In the case of relatively tall structures, such as the bridge investigated here, the response may be influenced by geometric non-linearity induced by the weight of the deck as
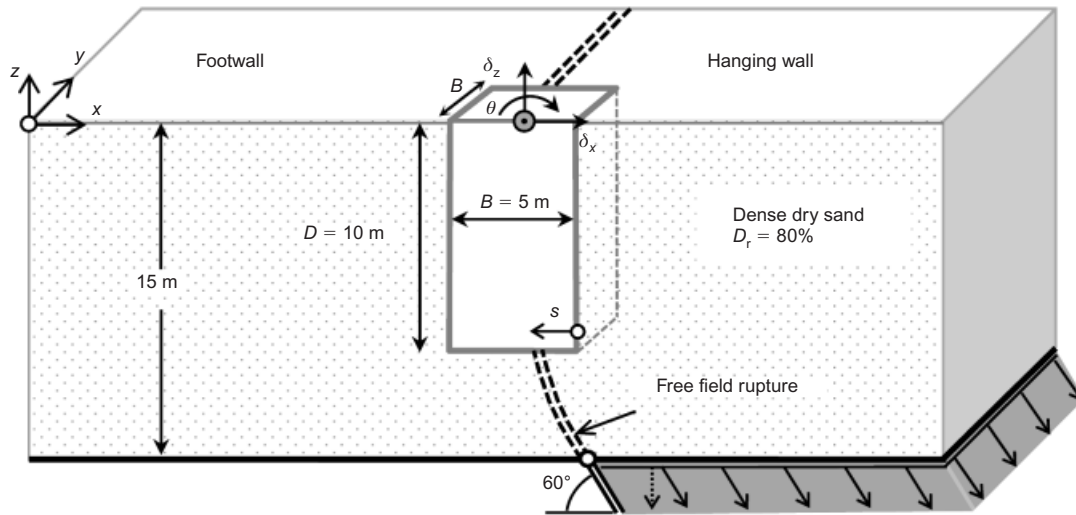
Fig. 2. Schematic diagram of studied problem, indicating basic parameters and dimensions at prototype scale. Free-field rupture indicates rupture path in absence of caisson foundation

the pier rotates (the P–δ effect). In an attempt to isolate the role of P–δ effects, two different systems were considered: (a) a caisson foundation with a centre of mass at mid-embedment depth carrying the dead load of the bridge (i.e. ignoring P–δ effects); and (ii) a caisson–pier system, in which a mass equivalent to the deck was placed with a centre of mass 15 m above soil level, which was supported by an identical caisson foundation. Because of space limitations, the present paper focuses on the response of the caisson foundation without the pier, and the role of P–δ effects will be presented in a future publication.

Centrifuge testing

A series of centrifuge model tests were conducted in the beam centrifuge of the University of Dundee at an operational acceleration of 100g. Consequently, a scale factor of $N = 100$ was applied to all dimensions shown in Fig. 2 (e.g. Schofield, 1980). The experimental study aimed at investigating the mechanisms of fault rupture–caisson interaction with regard to the caisson position relative to the fault. Three centrifuge test results are reported (tests ML-07, ML-08 and ML-10), where the caisson was placed at three different positions, as indicated in Table 1, together with one test without a foundation (test ML-06) to give the 'free-field' fault position.

The location of the caisson relative to the outcropping fault rupture is expressed by the parameter s, which is defined as the distance between the caisson right corner and the point at which the free-field (unperturbed) fault rupture would cross the foundation base (Fig. 2). In other words, s indicates the point where the fault rupture would interact with the caisson if fault rupture–caisson interaction did not take place to alter the rupture path.

Instrumentation. The faulting process was simulated using a split box with internal dimensions $x = 655 \cdot 9$ mm, $y = $

Table 1. Centrifuge testing programme

Test ID	Caisson position, s/B	Soil density, D_r: %
ML-06	–	77·5
ML-07	0·78	70·0
ML-08	0·28	74·6
ML-10	0·58	76·0

500 mm and $z = 220$ mm, contained within a centrifuge strongbox. Cole & Lade (1984) first used a split box (i.e. a glass-walled box with a split base) to simulate rupture propagation through granular soil, and performed a series of small-scale, free-field rupture tests. Similar split containers have been used to investigate the behaviour of buried pipelines subjected to strike-slip faulting (Trautmann & O'Rourke, 1985; O'Rourke *et al.*, 2008; Abdoun *et al.*, 2009). The apparatus used for this study has been used in the past in a variety of similar faulting problems, and has been described in detail in El Nahas *et al.* (2006) and Bransby *et al.* (2008a).

The moving part of the box was made to translate downwards, using a hydraulic actuator, to create normal-type faulting with a dip angle of 60° at the base of the soil model (standing for bedrock). Fault deformation was applied during spinning at 100g in a controllable, progressive, quasi-static manner, reaching base dislocations of around 2·5 m (at prototype scale). A single linear variable differential transducer (LVDT) was placed vertically on the rigid moving part of the split box to give direct measurement of the vertical component of fault displacement (throw) during testing. This was used to monitor the progress of fault actuation during the test, and to validate the image analysis results.

A digital camera was used to take pictures of the model from a fixed position inside the centrifuge 'gondola'. Approximately 100 pictures per test were taken at progressively increasing fault displacements. The photographic data were then analysed using the Geo-PIV program, written by White *et al.* (2003), to calculate caisson displacements and the shear strains developed within the soil.

Model preparation. A photograph of the centrifuge test model inside the strongbox is shown in Fig. 3. Because of the time limitations involved in centrifuge testing, the small-scale model was made in such a way that the response of the caisson on its own could be studied at the same time as the response of the caisson–pier system during each test. However, the two models were placed at a large enough horizontal distance so that caisson-to-caisson interaction can be considered negligible.

The 150 mm deep (i.e. 15 m at prototype scale) soil layer was prepared by dry air pluviation of Fontainebleau sand (Gaudin, 2002). The sand was pluviated from a specific height (250 mm from the bottom of the box), and a sieve
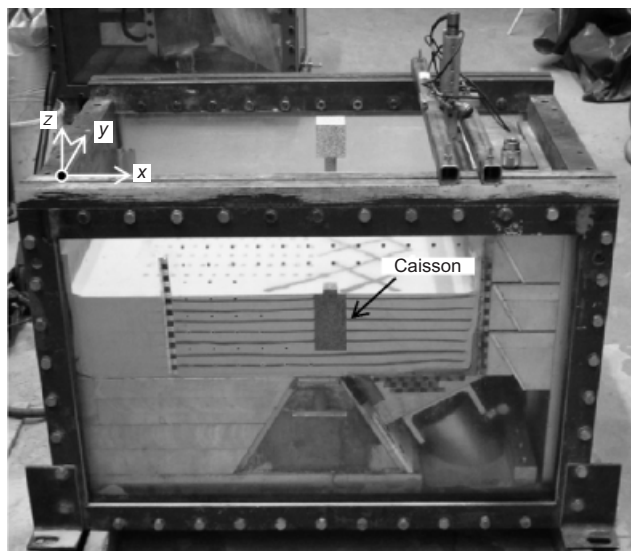
Fig. 3. Photograph of model and fault rupture apparatus used in centrifuge testing

(with 2 mm aperture) was used to control the mass flow rate, aiming to give a uniform density of 80% ($\gamma = 16 \cdot 11$ kN/m³). The density of the soil as measured after each test is given in Table 1. A series of direct-shear tests were conducted to investigate the soil stress–strain and volumetric behaviour. For a mean value of relative soil density $D_r = 80\%$ the peak and residual friction angles of soil were measured as $\phi_p = 37°$ and $\phi_{cs} = 31°$ at a normal effective stress representative of the middle of the soil depth (i.e. $\sigma'_v = 120$ kPa for depth, $z = -7 \cdot 5$ m). The dilation angle ψ, which depends significantly on the effective stress (Bolton, 1986), was measured as approximately 10° for the same normal effective stress.

After pluviating the first 50 mm of soil, the foundation base level was reached and the caisson model was placed at its designated position. The foundation was placed carefully, achieving minor initial displacements, to face the Perspex window of the box. Thereafter, the remaining 100 mm of soil was pluviated in the same way. It should be noted that the Perspex acts as a plane of symmetry, and hence the caisson dimensions perpendicular to the Perspex face were half the prototype values.

Former studies (e.g. Bransby et al., 2008a; Anastasopoulos et al., 2009) have indicated the significant effect of the foundation bearing pressure on the mechanisms of fault rupture–caisson interaction. Hence, although the bridge pier is in this particular case simulated in a simplified manner by the caisson only, it was considered essential to retain the bearing pressure carried by the foundation at a realistic level. Therefore the caisson model was made of steel, and had the same total weight as the pier model, carrying a vertical load of 20·11 MN in prototype scale.

Regarding the soil/caisson interfaces, the aim was to make them rough enough to simulate the concrete–soil interface realistically. For this purpose, the steel surfaces (except the side that faced the Perspex) were needle-gunned. The frictional properties at the interface were then measured by direct-shear tests performed on similar needle-gunned steel specimens. The interface friction angle (δ) on the caisson–soil interface was measured as 19·8° at peak and 17° at critical-state conditions.

Finite-element modelling
Former studies have shown that the finite-element (FE) method can quite satisfyingly simulate the phenomenon of

fault rupture propagation in the free field (e.g. Bray et al., 1994b; Anastasopoulos et al., 2007; Loukidis et al., 2009) and during fault–foundation interaction, at least as far as surface foundations are concerned (Anastasopoulos et al., 2009). Because of a lack of experimental data, the effectiveness of the FE method has not been proven for deep foundations. Having conducted innovative experimental work to probe the mechanisms of fault rupture interaction with embedded–caisson foundations, the opportunity arose to question whether the particular problem can also be adequately fitted in the limits of an unavoidably simplified numerical method. To this end, the methodology of Anastasopoulos et al. (2007) was appropriately adapted to the problem investigated in this paper.

To simulate the response of the square caisson realistically, three-dimensional (3D) modelling of the problem is required. The FE code ABAQUS was employed for this purpose. The model dimensions were chosen to be the same as the dimensions of the physical model at prototype scale. Fig. 4 shows the geometry, the boundary conditions and the main features of the FE mesh. It should be noted that only half of the model was simulated, taking advantage of the symmetry along the centreline of the foundation (which corresponds to the location of the Perspex front face in the centrifuge models). The geometry of the model fulfils the requirement of having an aspect ratio (length of model/ depth) greater than 4, as suggested by Bray et al. (1994b), to avoid parasitic boundary effects.

The Fontainebleau sand was modelled with 8-noded hexahedral continuum finite elements. Finite-element modelling of strain localisation, in conjunction with strain-softening constitutive modelling, may lead to mesh-dependence problems associated with the inherent limitation of the FE method in reproducing shear band formation and propagation within granular materials (e.g. Pietruszezak & Stolle, 1985). Gudehus & Nubel (2004) suggest that very fine FE meshes, with element width of the order of three times the mean grain size, are required to obtain mesh independence. However, it is impractical to implement mesh refinement of such level in real-scale complex problems (such as that investigated herein), given current computing power constraints.

Since the width of the FE shear band is equal to the element size (d_{FE}), d_{FE} should ideally be set equal to the width of the shear band. For the case of sand, the shear band thickness is known to depend on the particle size (Mühlhaus & Vardoulakis, 1987; Muir Wood, 2002), and has been observed to range from 10 to 18·5 times the mean grain size (typically estimated as $16d_{50}$). Hence a maximum element size $d_{FE} \approx 16d_{50}$ would be required to simulate the localisation of shear strains in the field. However, the present study deals primarily with the numerical simulation of centrifuge
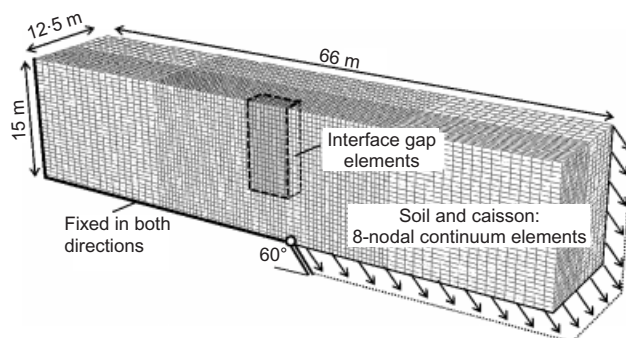

Fig. 4. Three-dimensional finite-element mesh used in numerical analyses, showing geometry, boundary conditions and some modelling details

experiments, and given that the grain size is not scaled down in centrifuge modelling, the element size should be increased accordingly so as to maintain similarity between experiment and analysis. Specifically, for the case of Fontainebleau sand ($d_{50} = 0.3$ mm), the maximum required element width would be $d_{FE} = N \times 16d_{50} \approx 0.5$ m. Consequently, $d_{FE} = 0.5$ m was selected in this study as an optimal compromise between simulation realism and computational efficiency. The ensuing scale effects were accounted for in the calibration of the constitutive soil model, as explained in the following section.

The FE mesh was finer in the central part of the model, with a uniform element size (0.5 m $\times$ 0.5 m $\times$ 0.5 m), which became coarser at the two edges (1 m $\times$ 0.5 m $\times$ 0.5 m), where limited deformation was expected. The bottom boundary represented the interface between soil layer and rigid bedrock. Hence it was split into two parts: one that remained stationary and the other that followed the hanging wall movement of the fault. The analysis was conducted in three steps. Initially, the geostatic conditions (including application of soil self-weight) were activated in step 1, followed by gravity loading (with the dead load of the bridge superstructure) in step 2. The differential fault displacement was then applied in step 3 to the right-hand part of the model, as shown schematically in Fig. 4, in adequately small, quasi-static analysis increments.

Soil constitutive modelling. The elasto-plastic constitutive relation described by Anastasopoulos *et al.* (2007) was used and encoded in ABAQUS through a user subroutine. This assumes elastic pre-yield soil behaviour defined by the secant shear modulus G_s, which was increased linearly with soil depth. The Mohr–Coulomb failure criterion was used to define failure, accompanied by an isotropic strain-softening law, which degraded the friction (ϕ) and dilation (ψ) angles linearly with octahedral plastic shear strain γ_{oct}^{pl}, according to the relationships

$$\phi; \psi =$$
$$\begin{cases} \phi_p - \dfrac{\phi_p - \phi_{cs}}{\gamma_f^{pl}} \gamma_{oct}^{pl}; \ \psi_p \left(1 - \dfrac{\gamma_{oct}^{pl}}{\gamma_f^{pl}}\right) & \text{for } 0 \leqslant \gamma_{oct}^{pl} < \gamma_f^{pl} \\ \\ \phi_{cs}; 0 & \text{for } \gamma_{oct}^{pl} \geqslant \gamma_f^{pl} \end{cases}$$
$$(1)$$

where ϕ_p and ϕ_{cs} are the peak and critical-state soil friction angles; ψ_p is the peak dilation angle; and γ_f^{pl} is the octahedral plastic shear strain at the end of softening. Constitutive model parameters were calibrated based on the results of the direct-shear tests. A simplified scaling method, described in detail and validated by Anastasopoulos *et al.* (2007), was implemented to extrapolate the stress–strain results determined from laboratory element testing to the centrifuge scale and the equivalent prototype used in the analysis. More specifically, the previously described scaling effect of the modelling parameters (i.e. the element width and/or the centrifuge scale) on the shear band width was counterbalanced by an equivalent scaling in the post peak stress–strain relationship. That is, γ_f^{pl} is calculated as

$$\gamma_f^{pl} = \gamma_{p(lab)}^{pl} + \frac{\gamma_{f(lab)}^{pl} - \gamma_{p(lab)}^{pl}}{\lambda} \qquad (2)$$

where $\gamma_{p(lab)}^{pl}$ and $\gamma_{f(lab)}^{pl}$ are the plastic shear strain at peak and at the end of softening respectively, as measured through shearbox testing. The factor λ was introduced to account for

scale effects, and is defined as the ratio of the shear band width in the prototype to the FE width ($\lambda = d_{FE}/d_B$).

Since the objective was to simulate centrifuge model tests, the parameter λ was calculated for the equivalent prototype with $d_B = N \times 16d_{50}$, giving for this particular case $\lambda \approx 1$. Obviously, if the aim was to model reality, or a full-scale laboratory experiment, N should be taken to be equal to 1. Table 2 summarises the values assigned to the input parameters of the soil model.

Modelling the caisson and soil/caisson interface. Three-dimensional continuum elements were also used for the caisson, which was assumed to be linearly elastic with typical stiffness properties for steel. The soil/caisson interface was modelled using contact elements to allow sliding and/or detachment (loss of contact) to occur. In order to simulate the centrifuge experiments, the interface properties were calibrated to match the frictional properties of the steel/sand interface as measured in the direct-shear tests. As the studied problem involves interaction of the foundation with a propagating shear band (fault rupture), it was assumed that residual conditions take place on the soil/caisson interface. In addition, because large strains were of greatest interest, the soil/caisson interface was modelled as a rigid–perfectly plastic interface with failure defined as

$$\tau = \sigma' \tan \delta_{cs} \qquad (3)$$

where δ_{cs} ($= 17°$ in these analyses) is the friction angle of the steel/sand interface at critical-state conditions. Since the difference between the measured δ_{peak} and δ_{cs} values is not large, this simplification is believed to be reasonable.

CHARACTERISTIC RESULTS
Fault rupture in the free field
The free field test (test ML-06) is discussed first as a reference for the following interaction tests. Fig. 5 highlights the failure mechanisms that develop within the soil during the evolution of the faulting process, and compares the centrifuge test results with the numerical analysis. Soon after initial application of fault loading, an initial very steep localisation of shear deformation (L1 in Fig. 5(a)) appears in the centrifuge test model, and propagates up to about one-third of the soil depth. Increasing bedrock fault offset h leads to formation of a second less steep failure plane (L2), which propagates up to the soil surface with little additional fault throw. By a fault throw of $h = 1.2$ m (Fig. 5(a)), the fault deformation is localised upon this distinct plane (L2), and a quite sharp scarp forms on the soil surface.

The numerical simulation captures the generation and general shape of the two aforementioned rupture planes. However, it underestimates the extent of deformation occur-

Table 2. Constitutive model input parameters

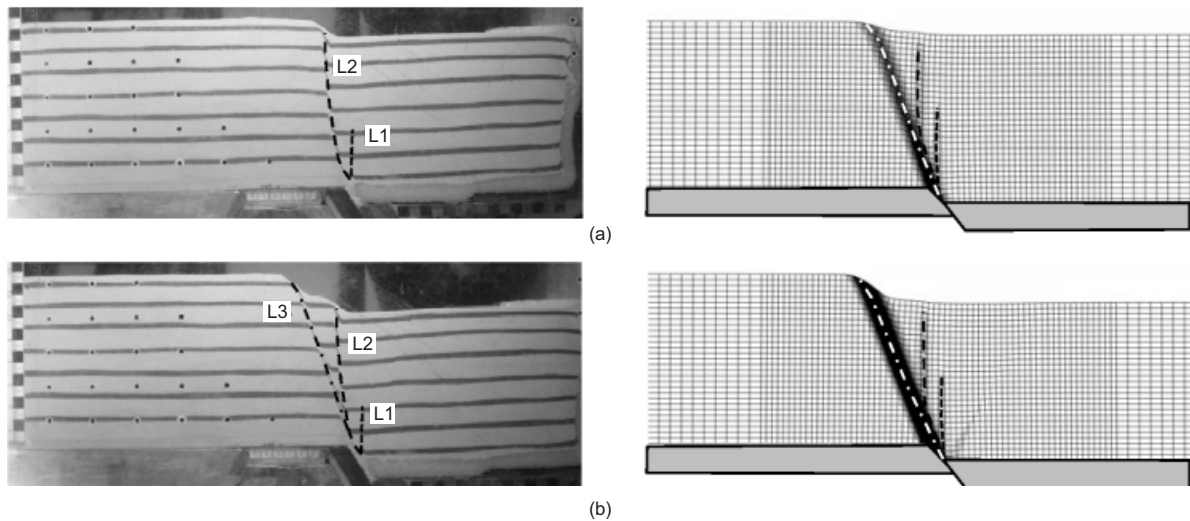| Parameter	Value
Unit weight, γ: kN/m^3	16·11
Secant shear modulus, G_s: kPa	1200z
Poisson's ratio, ν	0·3
Friction angle, ϕ_p: degrees	37
Friction angle, ϕ_{cs}: degrees	31
Dilation angle, ψ_p: degrees	10
Dilation angle, ψ_{cs}: degrees	0
Strain, γ_{yield}	0·011
Strain, γ_{peak}^{pl}	0·017
Strain, γ_f^{pl} ($N = 100$)	0·17

Fig. 5. Photographs of deformed soil model captured during free-field centrifuge test (ML-06) compared with finite-element deformed mesh with superimposed plastic strain for two different amplitudes of fault throw (bedrock offset): (a) $h = 1\cdot2$ m; (b) $h = 2\cdot5$ m

ring along the L2 failure plane. The analysis shows an early mobilisation of a final, shallower mechanism (L3), which also appears in the centrifuge test (Fig. 5(b)), but for a significantly larger bedrock offset h. This difference between experiment and analysis may be attributed to the approximate simulation of soil behaviour and scale effects, or may just be a result of natural variability in the experiments.

During the centrifuge test, a camera disconnection problem lost data for fault displacements larger than $1\cdot2$ m. Nevertheless, the test was continued to a maximum throw of $2\cdot5$ m, and a final image was captured when connection with the camera was regained. This image is compared with the deformed FE mesh at the corresponding load increment in Fig. 5(b), demonstrating a more satisfactory comparison. At this level of loading a final failure mechanism (L3), corresponding to critical-state conditions, has mobilised. Although no data are available between $h = 1\cdot2$ m and $2\cdot5$ m, comparing the corresponding photographs (Figs 5(a) and 5(b)) reveals that almost no additional deformation has taken place along localisation plane L2. Hence for $h > 1\cdot2$ m most of the shear deformation localised along L3, which finally became the main rupture plane. Consequently, it can be claimed that the comparison between analysis and experiment is quite acceptable for $h > 1\cdot2$ m.

It is also important to note that the above described experimental and numerical results appear to be in qualitative agreement with former experimental studies (Cole & Lade, 1984; Bransby *et al.*, 2008b) and field observations (Bray *et al.*, 1994a) of normal fault rupture propagation in the free field. These studies indicate that normal faults tend to 'refract' on the soil/bedrock interface, and propagate to the surface at increased dip angles. Moreover, they commonly develop steeper secondary ruptures (L1 and L2 in this case) at low throw values, which bend over the hanging wall (as L2 does).

Fault rupture–caisson interaction

This section presents the mechanisms of fault rupture–caisson interaction for three different caisson positions relative to the outcropping fault rupture.

Fault rupture at $s/B = 0\cdot78$ (test ML-07). In this test the caisson was positioned so that the free-field rupture would

strike its base in the vicinity of its footwall-side (left) corner. A selection of images captured at different increments of fault loading is shown in Fig. 6(a). Shortly after initiation of the faulting process, at $h = 0\cdot3$ m, a distinct failure plane appears to propagate from the bedrock fault discontinuity towards the footwall (left) side of the caisson base. Intersecting with the corner of the caisson, the fault rupture emerges on the ground surface, deviating approximately $1\cdot5$ m to the left of its free-field outcrop. Additional fault displacement ($h = 1\cdot0$ m) results in the formation of a shallower localisation in a similar way to the free-field case. The general resemblance in the failure pattern between this test and the previously described free-field test indicates the limited effect of the presence of the caisson in this case. Furthermore, the corresponding shear deformation contours (Fig. 6(b)) suggest that there is practically no deformation occurring outside the two distinct rupture planes. Hence the caisson and the soil on the hanging wall seem to translate rigidly, with no evidence of distress

The numerically computed shear strain contours (Fig. 6(c)) demonstrate the general agreement between analysis and experiment for all stages of fault loading. Although the numerical analysis predicts more extensive interface slip occurring along the footwall-side (left) caisson sidewall, the general pattern of failure and the fault-outcropping position are captured with reasonable accuracy. This is also supported by the satisfactory comparison of surface vertical displacements shown in Fig. 7.

Figure 8 illustrates the performance of the caisson with respect to the applied fault throw in terms of displacements (δ_x and δ_z) and rotation (θ) of the caisson measured at a reference point at the centre of the foundation at ground surface level (see Fig. 2). The figure confirms the previous argument regarding the limited distress of the caisson, which experiences far less rotation of only approximately $1\cdot2°$ for a fault throw of $2\cdot5$ m. The numerical analysis (also shown in Fig. 8) predicts with accuracy the translational displacements (δ_x and δ_z) of the caisson. The discrepancies are slightly larger in terms of caisson rotation θ, but the comparison is still quite satisfactory. In particular, the analysis predicts positive (anticlockwise) rotation of the caisson for small amplitudes of bedrock dislocation ($h < 0\cdot3$ m), which was not observed in the experiment. This disagreement between analytical and experimental results could be attributed to the assumption of linear elastic soil behaviour before soil yielding.

$h = 0.3$ m $h = 1.0$ m $h = 2.0$ m

(a)

(b)

(c)

Plastic shear strain: %

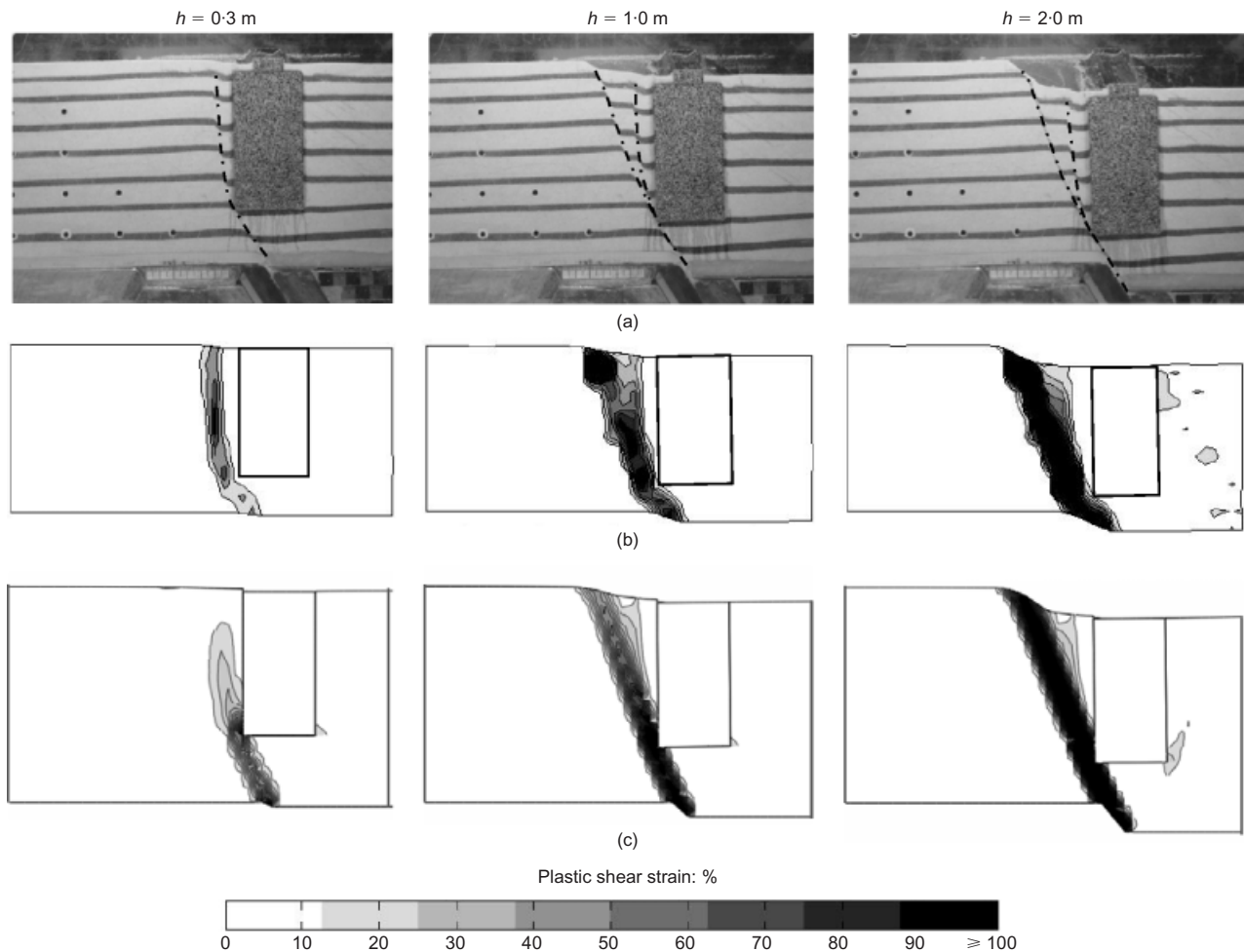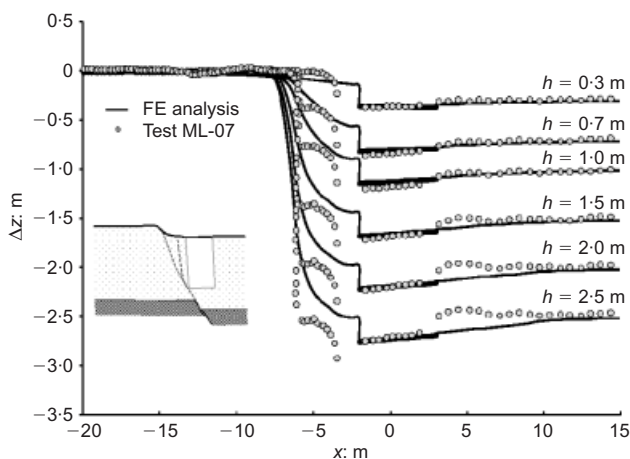0   10   20   30   40   50   60   70   80   90   ≥ 100

Fig. 6. Fault rupture–caisson interaction for different amplitudes of fault throw for $s/B = 0.78$ (test ML-07): (a) centrifuge test model images and (b) contours of shear strains developed within soil in centrifuge test (from particle image velocimetry (PIV) analysis), compared with (c) finite-element deformed mesh with superimposed plastic shear strains. Note that for purely technical reasons PIV results are shown for a slightly smaller region of the model

Fig. 7. Fault rupture–caisson interaction for different amplitudes of fault throw for $s/B = 0.78$ (test ML-07): vertical displacement profile at ground surface at different stages of faulting, and comparison with numerical results

Fault rupture at $s/B = 0.58$ (test ML-10). In this test the free-field fault rupture would have struck approximately in the middle of the caisson base ($s/B = 0.58$). Images of the centrifuge test model at different fault throw values (Fig. 9(a)) and corresponding shear strain contours (Fig. 9(b))

indicate a more subtle failure mechanism, compared with the previous test. The fault is again diverted to the footwall (left) side of the caisson, and a quite steep localisation (L1) is mobilised, emerging at the surface for $h = 0.5$ m. However, at the same time a second localisation (L2) forms at the other (hanging wall) side of the caisson. Initiating from the base dislocation point, it intersects with the hanging wall (right) caisson corner and propagates along the hanging wall (right) sidewall up to about two-thirds of the soil depth. This secondary rupture becomes inactive for larger fault throws, and never reaches the soil surface.

Soil failure around the caisson and underneath its base (Fig. 9(b)) leads to clockwise (positive) caisson rotation. The consequent active-type failure conditions generated to the footwall (left) side of the caisson (which acts as a rotating retaining wall) are believed to have aggravated the strain field at this side. L1, which becomes the prevailing deformation plane for $h > 0.5$ m, is probably the result of interplay between the two different failure mechanisms.

Results from FE analysis (Fig. 9(c)) appear to be in qualitative agreement with the experiment. The bifurcation of the shear plane at the two sides of the caisson is captured numerically, although the extent of failure on the hanging-wall side for low fault displacements is underestimated. This is also indicated by the comparison of surface displacements shown in Fig. 10. The main discrepancy between analysis and experiment refers to the inclination of the main rupture plane (L1). The computed rupture plane propagates with a
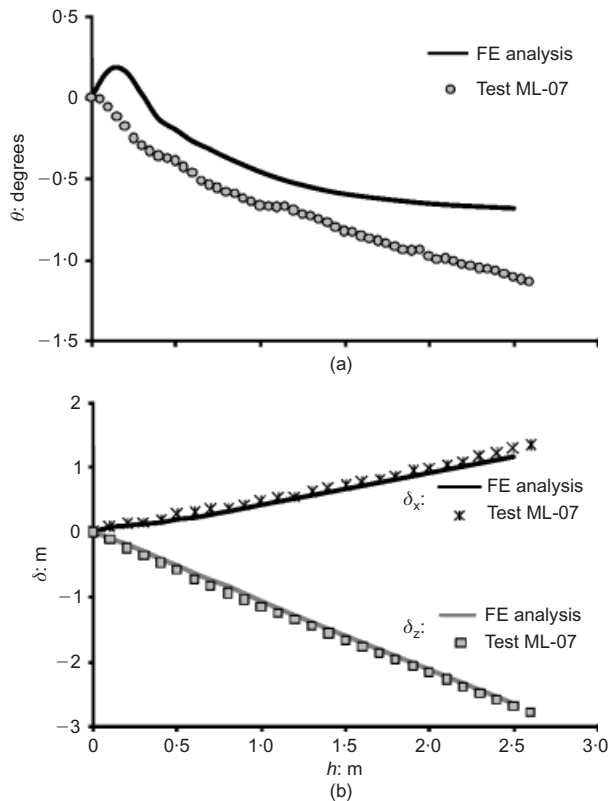
Fig. 8. Response of caisson foundation against applied fault displacement for $s/B = 0.78$ (test ML-07) and comparison with numerical results in terms of: (a) caisson rotation; (b) horizontal and vertical displacements at top of caisson (at base of pier)

shallower dip angle, and therefore outcrops about 2.5 m further away towards the footwall than observed experimentally.

In the model tests, significant sliding takes place at the soil/caisson footwall (left) sidewall interface for fault displacements exceeding 0.5 m (indicated by the dashed line in Fig. 9(a)). A gap (loss of contact between the soil and the caisson) appears in the vicinity of the caisson's top-left (footwall-side) corner, indicated by the discontinuity of surface displacement profiles in Fig. 10. This gap formation is also predicted by the numerical method, although its magnitude is underestimated. This discrepancy may be associated with the difference in the inclination of rupture L1, as a result of which the failure wedge predicted by the analysis is wider than in the experiment.

The caisson is evidently more distressed than in the previous test, and experiences significant rotation (Fig. 11(a)). Although the caisson rotation is well predicted for large values of bedrock dislocation ($h > 1.5$ m), the analysis underestimates the rotation due to smaller fault offsets. However, the analytical prediction is excellent in terms of translational displacements over the whole range of fault amplitudes (Fig. 11(b)). The disparity between analysis and experiment occurs because the lower part of the caisson displaces more in the analysis, which may be related to the earlier propagation of the secondary rupture L2 in the test compared with the analysis (see Fig. 9). Localisation L2 allows for some of the fault deformation to occur on the hanging wall (right) side of the caisson, causing greater rotation but at the same time limiting the translational movement of its base. It is also interesting to observe that the rate of caisson rotation accumulation with increasing fault displacement in the test reduces significantly for $h > 0.6$ m (observe the corresponding bend in Fig. 11(a)), when L2

becomes inactive and fault deformation propagates only along L1.

Fault rupture at $s/B = 0.28$ (test ML-08). This test, wherein the caisson base would have been crossed by the free field rupture near its right corner, gave the most intriguing interaction mechanisms.

Figure 12(a) displays a set of the centrifuge model test images, captured at different levels of fault displacement, and demonstrates a progressive type of failure associated with the interplay between different failure mechanisms. First, for $h = 0.5$ m, the caisson acting as a kinematic constraint forces the rupture to deviate significantly from its free-field path, actually changing orientation, and to propagate towards the hanging wall (right) caisson edge. Interestingly, L1 propagates at a dip angle greater than 90° (about 98°), contradicting the orientation of rupture in the bedrock, which probably explains why it only forms for a fault throw of approximately 0.6 m (recall that in the previous two tests the fault emerged on the surface for throws lower than 0.5 m).

Shear stresses develop along the right sidewall of the caisson, and its consequent clockwise rotation causes active-type stress conditions to take place on the other (left, hanging-wall) side of the caisson. An active failure wedge forms on the footwall (left) side of the foundation for $h = 1.0$ m, clearly indicated by the respective shear strain contours in Fig. 12(b). Soil failure on the footwall (left) side, as well as the soil distress underneath the foundation base due to its significant rotation, 'facilitate' the diversion of the rupture to the left (hanging-wall side) of the caisson, and a secondary rupture plane (L2) is mobilised. Thereafter, a rather subtle interaction mechanism is observed, involving the formation of active and passive failure wedges on the left (hanging-wall) and right (footwall) side of the caisson respectively, and fault propagation on both sides concurrently (see image for $h = 2.0$ m and the equivalent shear strain contours).

The numerically computed shear strain contours shown in Fig. 12(c) indicate that the numerical analysis captures the fault rupture–caisson interaction mechanisms closely, demonstrating excellent agreement with the experiment. Moreover, Fig. 13 demonstrates a fairly satisfactory comparison between analysis and experiment regarding the surface settlement profiles.

The extensive soil failure around the caisson (at both sides) provoked very large displacements (see Fig. 14). In particular, the rotation of the caisson after this test is more than two times larger than the rotation in the previous test, reaching about 12° for $h = 2.5$ m. Moreover, as in the previously reported test, a large gap appears at the footwall (left) side of the caisson (observe the sliding plane along the left sidewall highlighted in Fig. 12(a)). Again, the analysis underestimates the extent of this gap, as well as the surface gradient on the hanging-wall (left) side of the caisson, as indicated by the comparison of surface displacement profiles in Fig. 13. Despite this discrepancy, the analysis predicts with remarkable accuracy the response of the caisson in terms of displacements (rotational and translational) for all stages of fault loading (Fig. 14).

DISCUSSION OF INTERACTION MECHANISMS AND THE EFFECT OF THE FOUNDATION POSITION

The presence of the caisson foundation has been shown to modify the rupture path. In all three centrifuge model tests the caisson effectively diverted the fault rupture, and acted as a rigid boundary. However, the interaction mechanisms
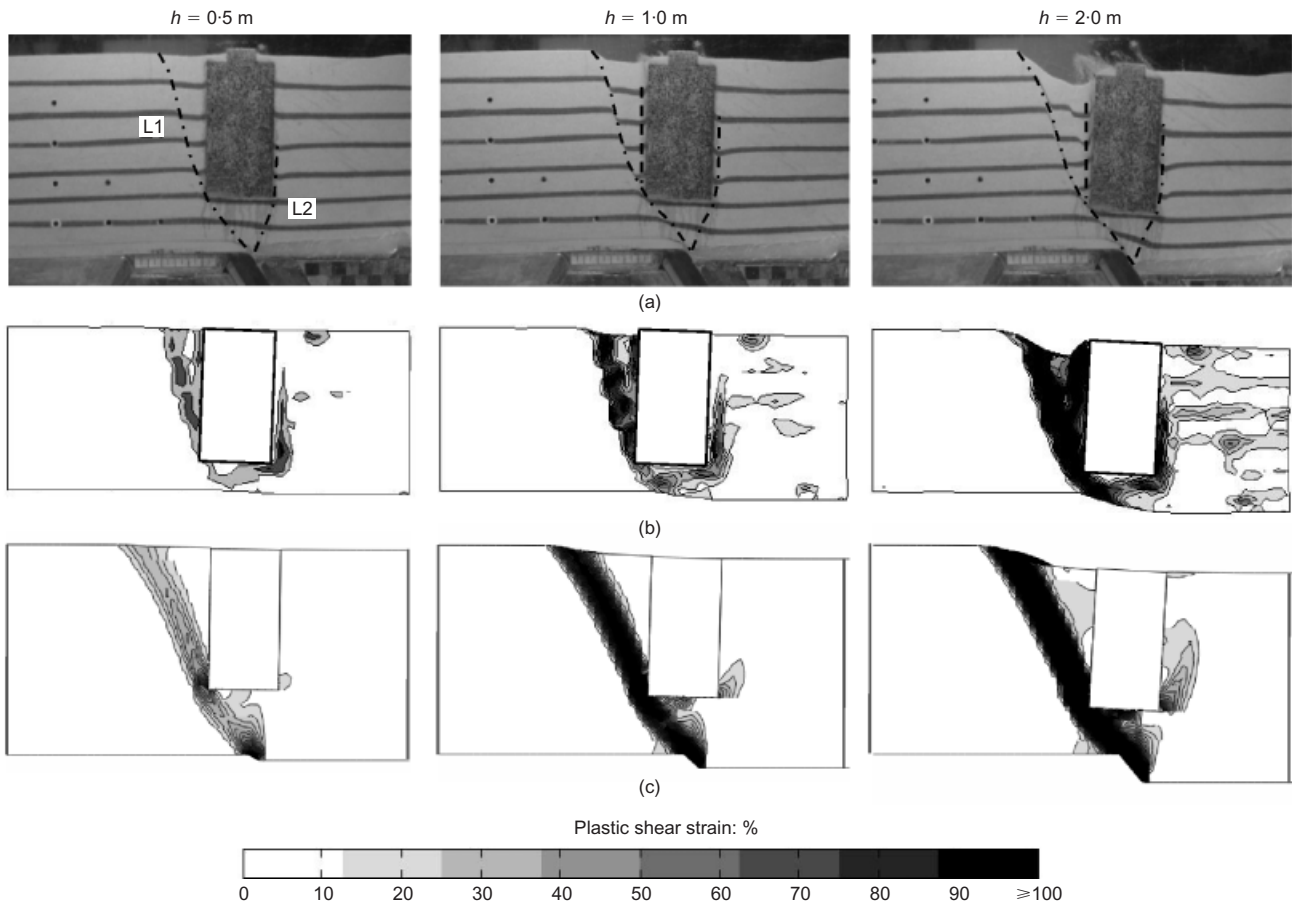
Fig. 9. Fault rupture–caisson interaction for different amplitudes of fault throw for $s/B = 0.58$ (test ML-10): (a) centrifuge test model images and (b) contours of plastic shear strains developed within soil in centrifuge test (from PIV analysis), compared with (c) finite-element deformed mesh with superimposed plastic shear strains. Note that for purely technical reasons PIV results are shown for a slightly smaller region of the model
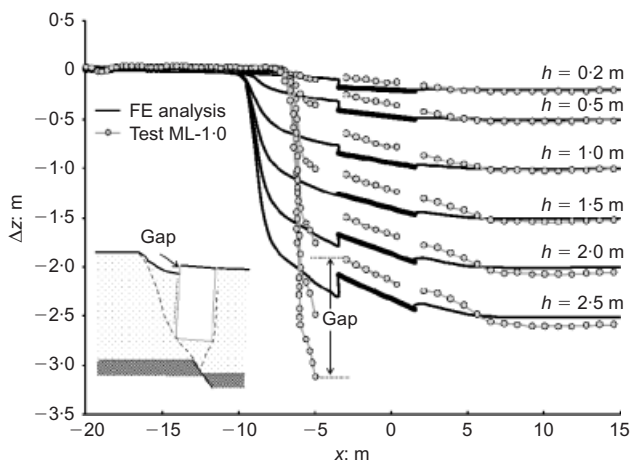

Fig. 10. Fault rupture–caisson interaction for $s/B = 0.58$ (test ML-10): vertical displacement profile at ground surface for different stages of faulting and comparison with numerical results

and the consequences for foundation response varied significantly, and depended on the location of the caisson relative to the fault rupture. Depending on the distance s (i.e. the relative location), the displacement and rotation of the caisson was excessive in some cases and minimal in others. To gain further insight into the effect of the caisson position relative to the fault rupture, a parametric study was carried out numerically. This is presented in the following.

Figure 15 summarises the effect of foundation location on the response of the caisson for different levels of fault throw h as calculated from a series of 21 FE analyses, each with the foundation located at a different position, s, with respect to the fault. Three different interaction mechanisms can be identified, dividing the graph in three zones

(a) mechanism A, for $s/B < -0.4$
(b) mechanism B, for $-0.4 \leqslant s/B < 0.6$
(c) mechanism C, for $s/B \geqslant 0.6$.

The differences between the three interaction mechanisms are further elucidated in Fig. 16, in terms of caisson trajectories on the $\delta_x - \delta_z$ plane, and FE deformed meshes with superimposed plastic shear strain contours.

Mechanism A ($s/B < -0.4$; i.e. $s < -2$ m, since $B = 5$ m) takes place when the fault rupture 'grazes' the hanging-wall (right) sidewall of the caisson, missing its base by 2 m or more (A in Fig. 16). In this case, the rupture path is refracted on the rigid sidewall and deviated towards the hanging wall (to the right). The caisson remains on the footwall side (left) of the fault, and experiences limited distress (displacement and rotation) for all levels of fault throw h.

Mechanism B ($-0.4 \leqslant s/B < 0.6$; i.e. -2 m $\leqslant s < 3$ m, since $B = 5$ m) is prevalent when the fault rupture manages a 'direct hit' at the base of the caisson. As discussed in detail for test ML-08 ($s/B = 0.28$), the interaction of the caisson with the fault rupture is quite complex, involving

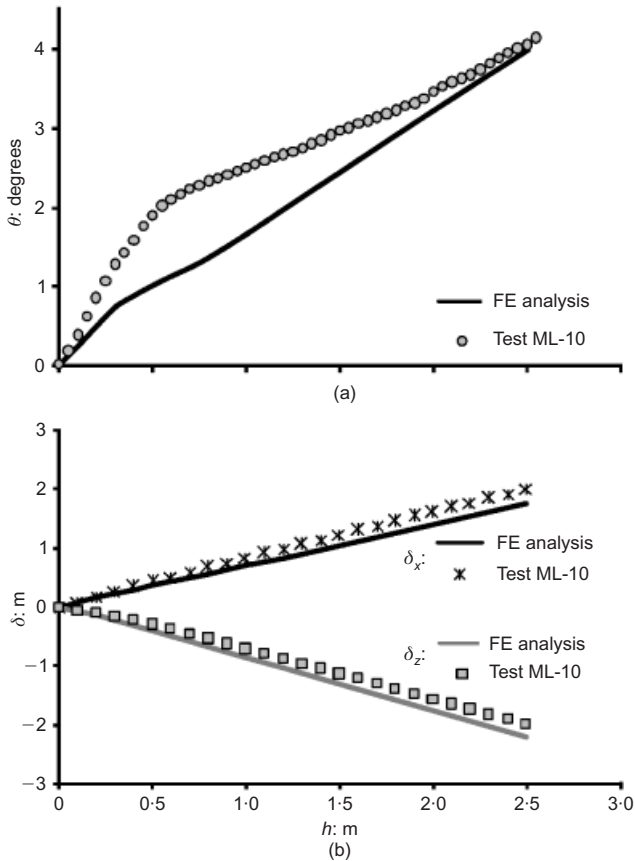(a) bifurcation of the shear zone along both sides of the caisson

Fig. 11. Response of caisson foundation against applied fault displacement for $s/B = 0.58$ (test ML-10) and comparison with numerical analysis in terms of: (a) rotation; (b) horizontal and vertical displacements at top of caisson (at base of pier)

(*b*) diffusion of the tectonic deformation underneath its base
(*c*) formation of an active failure wedge at the footwall (left) side of the caisson, owing to its substantial clockwise rotation (i.e. towards the hanging wall)
(*d*) formation of a passive-type failure wedge at the hanging-wall (right) side of the caisson (also due to the rotation).

This interaction case, which combines all of the above mechanisms, is probably the most detrimental in terms of caisson (and hence superstructure) distress, yielding significant rotation and vertical displacement (at the top of the caisson, i.e. at the base of the pier), combined with amplified horizontal displacements due to the clockwise rotation of the caisson.

Mechanism C ($s/B \geqslant 0.6$; i.e. $s > 3$ m, since $B = 5$ m) prevails when the fault rupture crosses the caisson close to its footwall (left) corner, or misses it completely on the footwall (left) side. As previously discussed in detail for test ML-07 ($s/B = 0.78$), the rupture can be diverted towards the footwall (to the left), and the caisson translates downwards, following the hanging wall, with only minor rotation. Fig. 16 confirms that the trajectory of caisson movement for this case follows the direction of faulting at bedrock after the main fault rupture has propagated to the soil surface. It is also interesting to observe that when the rupture intersects the caisson base at its footwall-side (left) corner, the rotational response is reversed (Fig. 15(c)), giving anticlockwise rotation (i.e. towards the footwall). This is explained by the intense soil yielding (associated with the rupture zone) beneath the footwall-side (left) corner of the caisson, which leads to loss of support, causing loss of balance and anti-clockwise rotation.

DISCUSSION OF MESH DEPENDENCE AND SCALE EFFECTS: LIMITATIONS

Combining centrifuge modelling and FE analysis to study fault rupture propagation in granular materials involves scale effects in both experiment and numerical simulation. A two-fold modelling problem is encountered: (i) in the centrifuge the shear band width is magnified by a factor equal to the gravity scale N; and (ii) in the FE analysis the shear band width is almost unavoidably controlled by mesh density.

In this study, the effect of these shortcomings, inherently related to the nature of the two modelling tools, was limited to some degree by the selection of a fine sand to use in centrifuge testing and the maximum practically possible refinement of the FE mesh. However, a sensitivity analysis considering both aspects of the problem was conducted in order to evaluate their possible impact on the derived conclusions. To this end, the fault rupture–caisson interaction problem was re-analysed for the case with caisson position, $s/B = 0.28$: (a) using a coarser mesh (with two times larger element width, $d_{FE} = 1.0$ m) to investigate the effect of mesh refinement; and (b) considering $N = 1$ (in the calibration of the soil constitutive model) aiming at modelling 'reality' rather than a conceptual prototype of the centrifuge model.

Figure 17 displays the results of this sensitivity analysis in terms of the fault rupture–caisson interaction mechanisms taking place at two different levels of fault displacement. The figure indicates that the element size affected the rupture zone thickness (compare Fig. 17(a) with Fig. 17(b)), showing a more diffused failure and hence a more even deformation of the soil surface in the case of the coarser mesh (Fig. 17(a)). The difference is less distinct when comparing the simulation of the centrifuge scale model with that of the real-scale problem (Figs 17(b) and 17(c)), with the only observable difference being the earlier propagation of the fault rupture in the 'real-scale' problem: observe in Fig. 17(c) that the rupture had already caused a distinct scarp in the surface for $h = 0.8$ m, which was not the case for the centrifuge scale model in Fig. 17(b). This was the expected outcome, given the linear scaling of the strain needed to cause critical-state conditions with respect to the shear band width. Despite these differences, it is important to notice that the general pattern of failure (the bifurcation of rupture on both sides of the caisson, the main rupture path and inclination, and the position of the surface fault outcrop) is the same in the three models.

The effect of mesh refinement and scaling on the performance of the same foundation is illustrated in Fig. 18. As expected, owing to the assumption made in the constitutive soil modelling regarding the soil behaviour before the shear band is formed, the response is the same in all three cases, and independent of scale for small values of fault displacement. However, scale effects do play a role in the response of the foundation to greater fault dislocations. The element size appears to affect mainly the caisson rotation (Fig. 18(b)) and much less its translational movement (Fig. 18(a)), showing generally larger displacements for the case of the coarser mesh.

The model scale (N) seems to play a more important role than the element size in the amount of caisson displacement. For this particular example the centrifuge scaling results in an overestimation of the caisson displacements, in comparison with the full-scale case. A sensitivity study should be extended to all possible fault–caisson positions to confirm the generalisability of this finding.

Overall, it can be claimed that although the presented results might be affected by scale effects quantitatively, the mechanisms of fault rupture–caisson interaction (which this study focused on) appear relatively insensitive to these effects. This gives confidence in the validity of the paper's
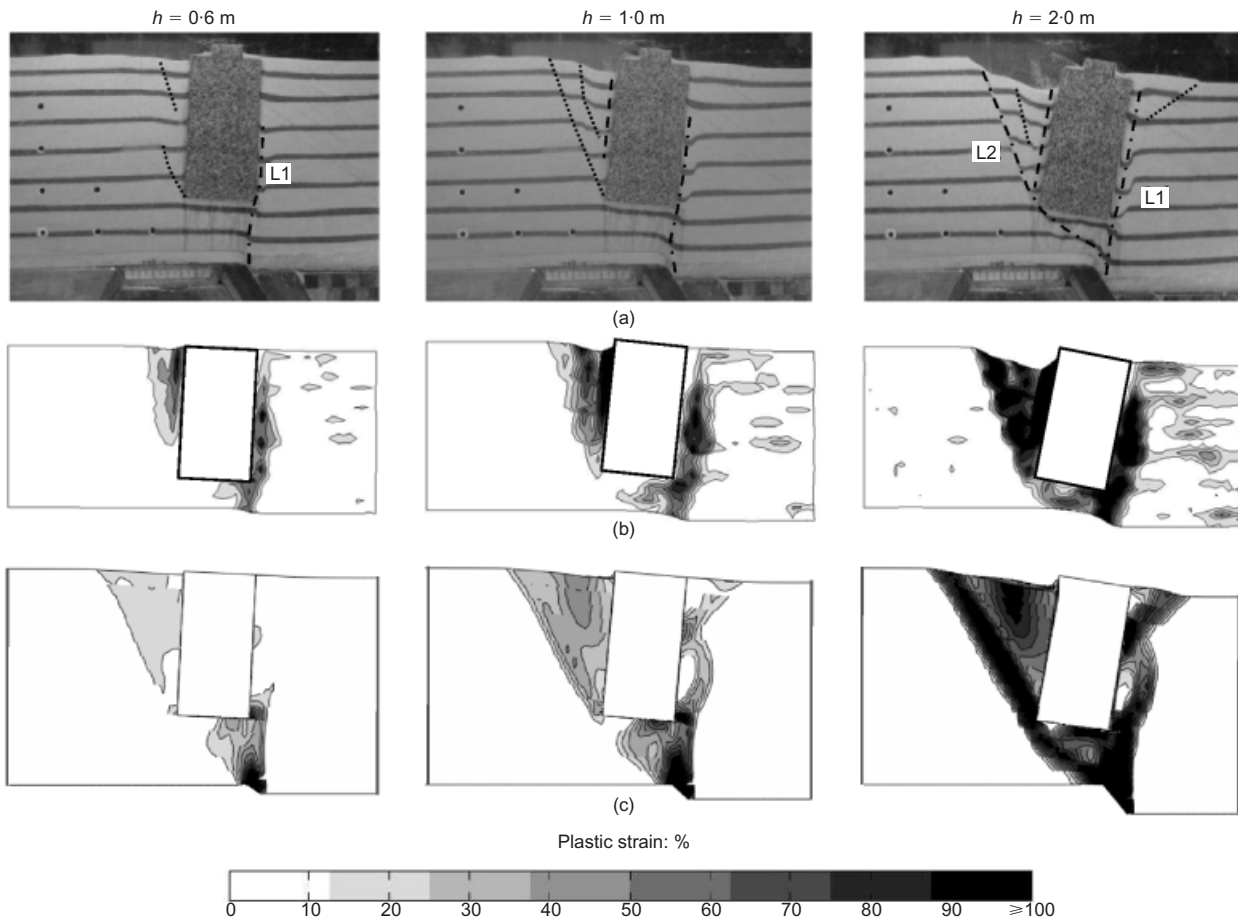
Fig. 12. Fault rupture–caisson interaction for different amplitudes of fault throw for $s/B = 0.28$ (test ML-08): (a) centrifuge test model images and (b) contours of shear strains developed within soil in centrifuge test (from PIV analysis), compared with (c) finite-element deformed mesh with superimposed plastic shear strains. Note that for purely technical reasons PIV results are shown for a slightly smaller region of the model
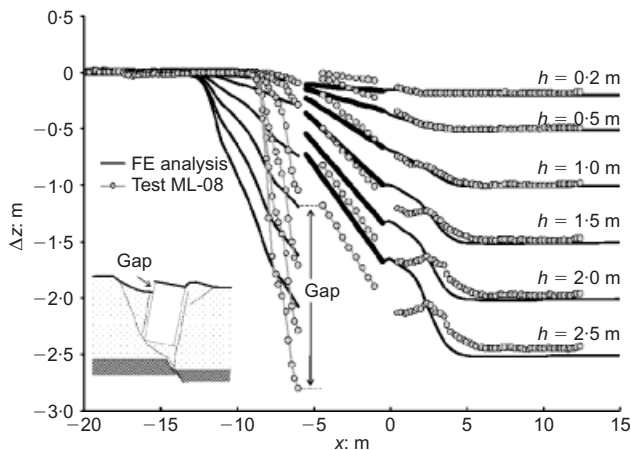

Fig. 13. Fault rupture–caisson interaction for $s/B = 0.28$ (test ML-08): vertical displacement profile at ground surface at different stages of faulting and comparison with numerical results

conclusions. Nevertheless, the reader should bear in mind that the approximate scaling method incorporated in the constitutive soil model is based on the following assumptions.

(*a*) Linear scaling is applied to the post-peak soil deformations with respect to the modelling scale (N, d_{FE}).
(*b*) The soil behaviour prior to the formation of the shear band is assumed to be independent of scale.

(*c*) In the centrifuge, the strain values at yield, at peak and at the end of softening are assumed to be the same as measured in direct-shear tests. This implies that the displacements required to cause soil yielding, mobilisation of strength and critical-state conditions are scaled up using conventional centrifuge scaling laws (White *et al.*, 1994). However, it should be noted that some evidence indicates that mobilisation displacements in the centrifuge are similar to those measured in a shearbox (Palmer *et al.*, 2003), implying that the hypothesis of the strain-scaling factor being unity may not apply for problems where shear-banding prevails.

CONCLUSIONS

This paper has presented a combined experimental and numerical study of normal fault rupture–caisson interaction. The effectiveness of the numerical analysis methodology employed was validated against the experimental results, and a parametric study was then conducted to shed more light in the effect of caisson location relative to the fault rupture. The key conclusions can be summarised as follows.

(*a*) Model tests have confirmed that the interplay of a caisson foundation with an outcropping normal fault rupture involves several different interaction mechanisms. The rigid caisson body acts as a kinematic constraint, always forcing the fault rupture to divert or bifurcate around the structure. This is an important difference compared with shallow foundations, where such mechanisms do not
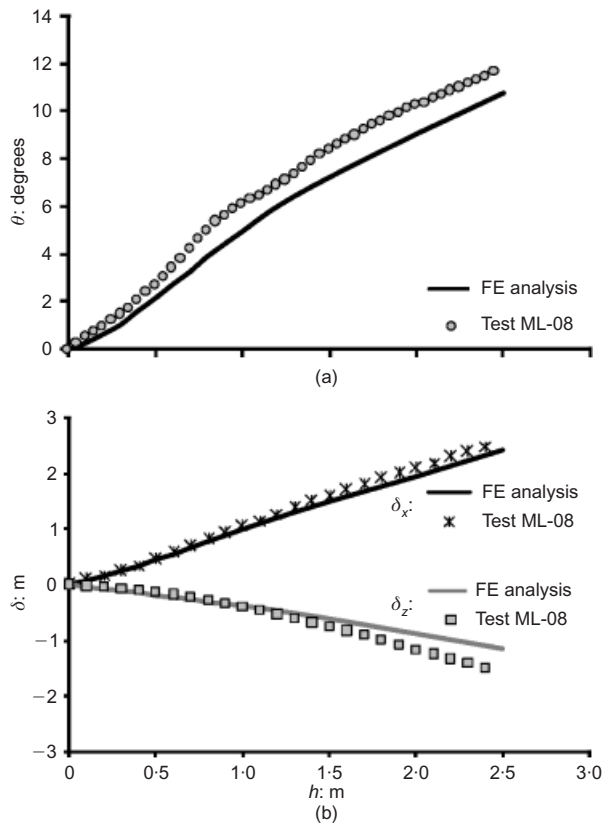
Fig. 14. Response of caisson foundation against applied fault displacement for $s/B = 0{\cdot}28$ (test ML-08) and comparison with numerical analysis in terms of: (a) caisson rotation; (b) horizontal and vertical displacements at top of caisson (at base of pier)

Fig. 15. Effect of location s of fault rupture on response of caisson, numerical parametric study: (a) vertical displacement, (b) horizontal displacements and (c) rotation for different levels of fault throw. Graphs are divided into three zones (A, B and C), corresponding to three different interaction mechanisms

always occur (e.g. a fault can emerge directly beneath a foundation and cause a gap to form; Anastasopoulos *et al.*, 2009).

(b) The numerical methodology employed to simulate fault rupture–caisson interaction has been shown to be quite effective. Despite the unavoidable shortcomings of the FE method in terms of modelling of strain localisation, the analysis captures the general pattern of fault rupture–caisson interaction mechanisms and the consequent caisson performance when compared with the experimental results. This gives confidence that the numerical method can be employed to study other similar problems, or be used as a design tool.

(c) The response of the foundation is very sensitive to its position relative to the fault rupture (Fig. 15).

(d) When the fault rupture 'grazes' the hanging-wall sidewall of the caisson (mechanism A), the rupture path is refracted and deviated towards the hanging wall, and the caisson experiences limited displacement and rotation.

(e) When the fault rupture manages a 'direct hit' at the base of the caisson (mechanism B), four different phenomena take place: (i) bifurcation of the shear zone around both sides of the caisson; (ii) diffusion underneath its base; (iii) formation of an active-type failure wedge at its footwall side; and (iv) formation of a passive-type failure wedge at its hanging-wall side. As a result, the caisson is subjected to significant rotation and vertical displacement, combined with amplified horizontal displacements. In the case of bridges, such displacements of the foundations can cause relative movement of consecutive piers, leading to seating problems and even collapse of the supported deck.
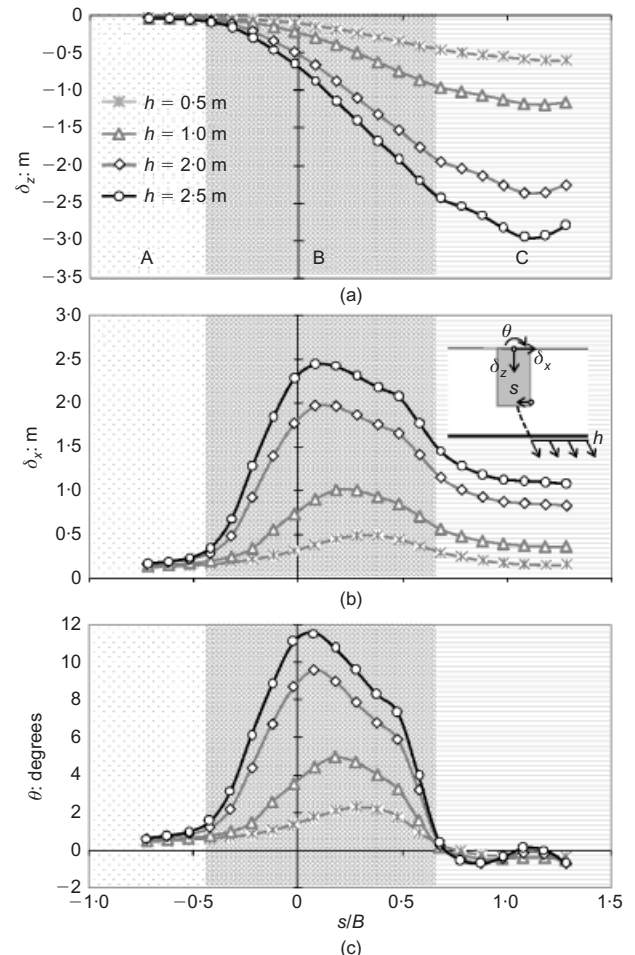
(f) When the fault rupture crosses the caisson close to its footwall corner (mechanism C), the rupture is diverted towards the footwall, and the caisson follows the downward displacement of the hanging wall, and is subjected only to minor rotation.

(g) Since the 'exact' location of a fault rupture cannot be known *a priori*, the design of structures (such as bridges) founded on caisson foundations should be performed on the basis of response envelopes of displacement and rotation, such as the one shown in Fig. 15. Although the results presented in this paper refer to a specific case, the key conclusions are believed to be of general validity.

ACKNOWLEDGEMENT

NOTATION

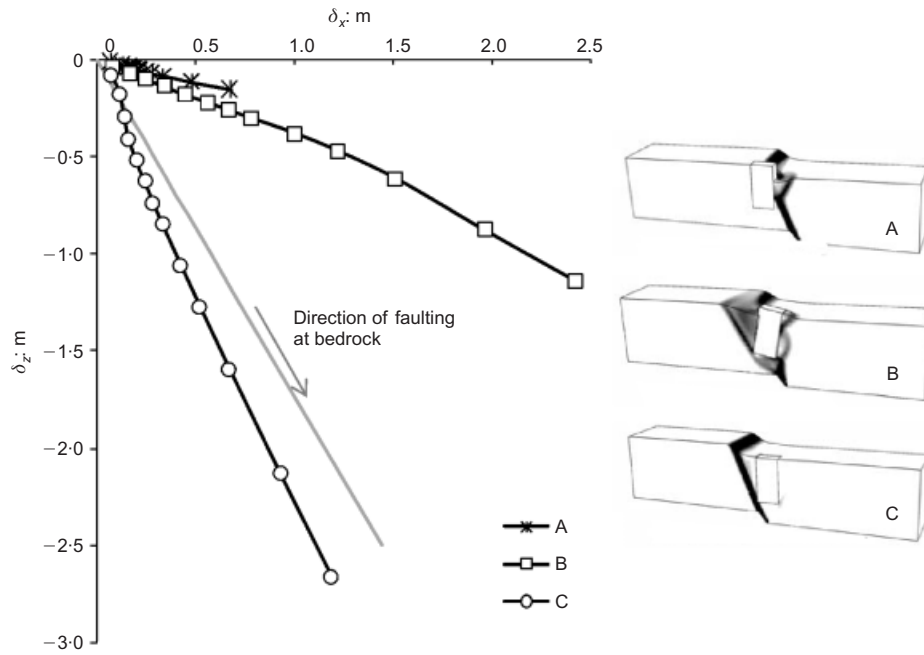|	
B	caisson width
D	caisson embedment depth
D_r	soil density
d_B	shear band width

Fig. 16. Effect of location s of fault rupture on the response of the caisson, numerical sensitivity analysis: horizontal against vertical displacement for three characteristic interaction mechanisms for cases A, B and C (results indicatively shown for $s/B = -0.32$, 0.18 and 0.88 respectively), along with the corresponding finite-element deformed meshes with plastic shear strain contours
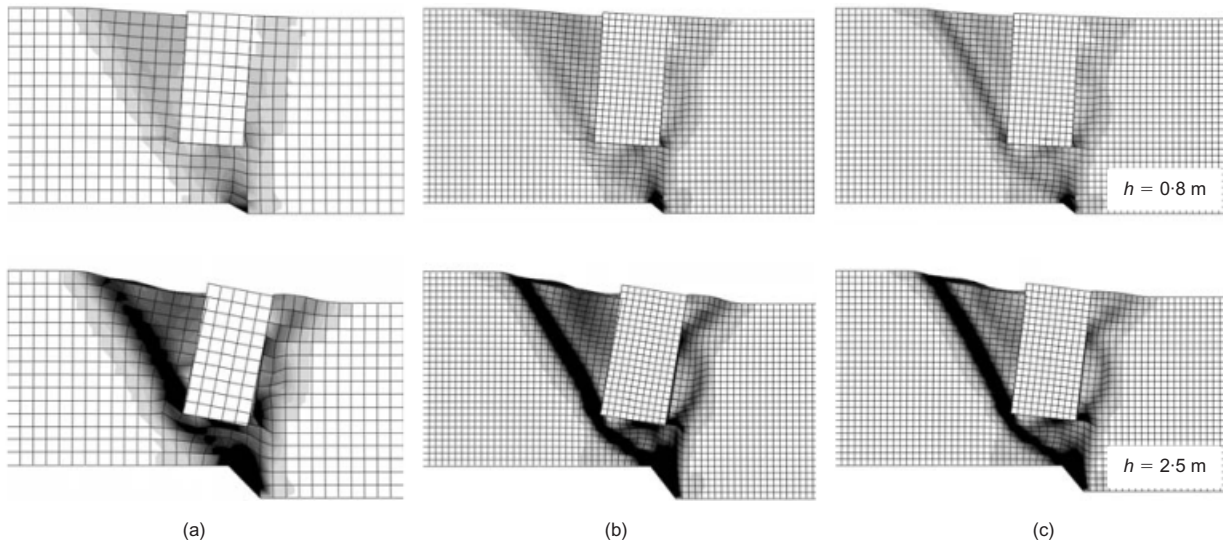

Fig. 17. Effect of mesh refinement and scaling on finite-element simulation of fault rupture–caisson interaction problem for $s/B = 0.28$ and two different fault offsets ($h = 0.8$ and 2.5 m). Finite-element deformed mesh with superimposed plastic shear strains for: (a) coarser mesh ($d_{FE} = 1.0$ m) at centrifuge scale ($N = 100$); (b) finer mesh ($d_{FE} = 0.5$ m) at centrifuge scale ($N = 100$); (c) finer mesh ($d_{FE} = 0.5$ m) at real scale ($N = 1$)

d_{FE}	finite-element size
d_{50}	mean grain size
G_s	secant shear modulus
h	vertical amplitude of fault displacement at bedrock (throw)
N	scale factor
s	relative to fault caisson position, defined as horizontal distance between caisson right corner and point where the free field rupture path crosses its base
Δz	vertical displacement of model surface along symmetry axis (Perspex)
γ	soil unit weight
γ_f^{pl}	octahedral plastic shear strain at end of softening
γ_{oct}^{pl}	octahedral plastic shear strain

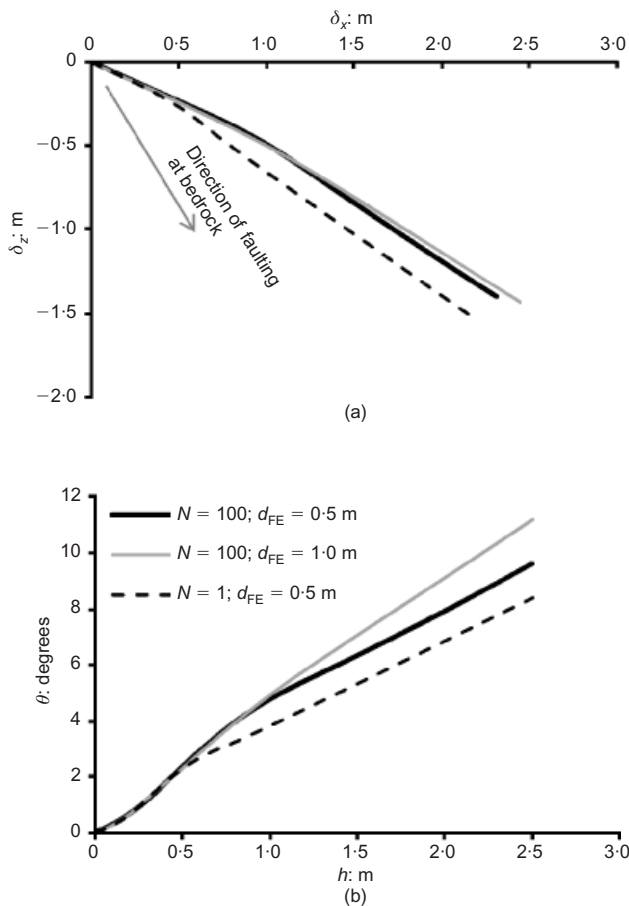|	
γ_{peak}^{pl}	plastic shear strain at peak
$\gamma_{p(lab)}^{pl}$, $\gamma_{f(lab)}^{pl}$	measured plastic shear strain at peak and end of softening
γ_{yield}	shear strain at yield
δ_{peak}, δ_{cs}	peak and critical-state friction angle at soil/caisson interfaces
δ_x, δ_z	horizontal and vertical components of caisson displacement with reference to middle point of its top side (soil surface level)
θ	caisson rotation
λ	ratio d_{FE}/d_B
ν	Poisson's ratio
σ'	effective normal stress
τ	shear stress
ϕ	friction angle of soil

Fig. 18. Effect of mesh refinement and scaling on caisson response for $s/B = 0.28$: (a) trajectories of caisson movement on x–z plane (with reference to middle point of caisson top side); (b) caisson rotation with respect to applied bedrock dislocation

ϕ_p, ϕ_{cs} friction angle of soil in peak and critical-state conditions
ϕ_{res} residual friction angle of soil
ψ dilation angle of soil
ψ_p, ψ_{cs} dilation angle of soil in peak or critical-state conditions

REFERENCES

Abdoun, T. H., Ha, D., O'Rourke, M. J., Symans, M. D., O'Rourke, T. D., Palmer, M. C. & Stewart, H. E. (2009). Factors influencing the behavior of buried pipelines subjected to earthquake faulting. *Soil Dynam. Earthquake Engng* **29**, No. 3, 415–427.

Ahmed, W. & Bransby, M. F. (2009). The interaction of shallow foundations with reverse faults. *J. Geotech. Geoenviron. Engng* **135**, No. 7, 914–924.

Anastasopoulos, I. & Gazetas, G. (2007a). Foundation-structure systems over a rupturing normal fault: Part I. Observations after the Kocaeli 1999 earthquake. *Bull. Earthquake Engng* **5**, No. 3, 253–275.

Anastasopoulos, I. & Gazetas, G. (2007b). Behaviour of structure–foundation systems over a rupturing normal fault: Part II. Analysis of the Kocaeli case histories. *Bull. Earthquake Engng*, **5** No. 3, 277–301.

Anastasopoulos, I., Gazetas, G., Bransby, M. F., Davies, M. C. R. & El Nahas, A. (2007). Fault rupture propagation through sand: finite element analysis and validation through centrifuge experiments. *J. Geotech. Geoenviron. Engng ASCE* **133**, No. 8, 943–958.

Anastasopoulos, I., Gazetas, G., Drosos, V., Georgarakos, T. & Kourkoulis, R. (2008). Design of bridges against large tectonic deformation. *Earthquake Engng Engng Vib.*, **7**, No. 4, 345–368.

Anastasopoulos, I., Gazetas, G., Bransby, M. F., Davies, M. C. R. & El Nahas, A. (2009). Normal fault rupture interaction with strip foundations. *J. Geotech. Geoenviron. Engng ASCE* **135**, No. 3, 359–370.

Bolton, M. D. (1986). The strength and dilatancy of sands. *Géotechnique* **36**, No. 1, 65–78, http://dx.doi.org/10.1680/geot.1986.36.1.65

Bransby, M. F., Davies, M. C. R., El Nahas, A. & Nagaoka, S. (2008a). Centrifuge modelling of normal fault–foundation interaction. *Bull. Earthquake Engng* **6**, No. 4, 585–605.

Bransby, M. F., Davies, M. C. R., El Nahas, A. & Nagaoka, S. (2008b). Centrifuge modelling of reverse fault–foundation interaction. *Bull. Earthquake Engng* **6**, No. 4, 607–628.

Bray, J. D., Seed, R. B., Cluff, L. S. & Seed, H. B. (1994a). Earthquake fault rupture propagation through soil. *J. Geotech. Engng* **120**, No. 3, 543–561.

Bray, J. D., Seed, R. B. & Seed, H. B. (1994b). Analysis of earthquake fault rupture propagation through cohesive soil. *J. Geotech. Engng* **120**, No. 3, 562–580.

Chang, K.-C., Chang, D.-W., Tsai, M-.H. & Sung, Y.-C. (2000). Seismic performance of highway bridges. *Earthquake Engng Engng Seismol.* **2**, No. 1, 55–77.

Cole, D. A. Jr & Lade, P. V. (1984). Influence zones in alluvium over dip-slip faults. *J. Geotech. Engng* **110**, No. 5, 599–615.

Dong, J. J., Wang, C. D., Lee, C. T., Liao, J. J. & Pan, Y. W. (2003). The influence of surface ruptures on building damage in the 1999 Chi-Chi earthquake: a case study in Fengyuan City. *Engng Geol.* **71**, Nos 1–2, 157–179.

El Nahas, A., Bransby, M. F. & Davies, M. C. R. (2006). Centrifuge modelling of the interaction between normal fault rupture and rigid, strong raft foundations. *Proc. Int. Conf. Physical Modelling in Geotechnics, Hong Kong*, 337–342.

Faccioli, E., Anastasopoulos, I., Callerio, A. & Gazetas, G. (2008). Case histories of fault–foundation interaction. *Bull. Earthquake Engng* **6**, No. 4, 557–583.

Gaudin, C. (2002). *Modelisation physique et numerique des écrans de soutenement: application a l'étude de l'effet d'une surcharge sur le sol soutenu*. PhD thesis, Universite de Nantes.

Gazetas, G., Pecker, A., Faccioli, E., Paolucci, R. & Anastasopoulos, I. (2008). Design recommendations for fault–foundation interaction. *Bull. Earthquake Engng* **6**, No. 4, 677–687.

Gudehus, G. & Nubel, K. (2004). Evolution of shear bands in sand. *Géotechnique* **54**, No. 3, 187–201, http://dx.doi.org/10.1680/geot/2004.54.3.187.

Loukidis, D., Bouckovalas, G. & Papadimitriou, A. G. (2009). Analysis of fault rupture propagation through uniform soil cover. *Soil Dynam. Earthquake Engng* **29**, No. 11–12, 1389–1404.

Mühlhaus, H.-B. & Vardoulakis, I. (1987). The thickness of shear bands in granular materials. *Géotechnique* **37**, No. 3, 271–283, http://dx.doi.org/10.1680/geot.1987.37.3.271.

Muir Wood, D. (2002). Some observations of volumetric instabilities in soils. *Int. J. Solids Struct.* **39**, Nos 13–14, 3429–3449.

O'Rourke, T. D., Jezerski, J. M., Olson, N. A., Bonneau, A. L., Palmer, M. C., Stewart, H. E., O'Rourke, M. J. & Abdoun, T. (2008). Geotechnics of pipeline system response to earthquakes. *Proc. 4th Geotechnical Earthquake Engineering and Soil Dynamics Congress Geotechnical Earthquake Engineering and Soil Dynamics, Sacramento, CA* (CD-ROM).

Palmer, A. C., White, D. J., Baumgard, J., Bolton, M. D., Barefoot, J., Finch, M., Powell, T., Faranski, A. S. & Baldry, J. A. S. (2003). Uplift resistance of buried submarine pipelines: comparison between centrifuge modelling and full-scale tests. *Géotechnique* **53**, No. 10, 877–883, http://dx.doi.org/10.1680/geot.2003.53.10.877.

Pamuk, A., Kalkan, E. & Ling, H. I. (2005). Structural and geotechnical impacts of surface rupture on highway structures during recent earthquakes in Turkey. *Soil Dynam. Earthquake Engng* **25**, Nos 7–10, 581–589.

Paolucci, R. & Yilmaz, M. T. (2008). Simplified theoretical approaches to earthquake fault rupture–shallow foundation interaction. *Bull. Earthquake Engng* **6**, No. 4, 629–644.

Pietruszezak, S. & Stolle, D. F. E. (1985). Deformation of strain softening materials. Part I: Objectivity of finite element solutions based on conventional strain softening formulations. *Comput. Geotech.* **1**, No. 2, 99–115.

Schofield, A. N. (1980). Cambridge University geotechnical centri-

fuge operations. *Géotechnique* **30**, No. 3, 227–268, http://dx.doi.org/10.1680/geot.1980.30.3.227.

Trautmann, C. H. & O'Rourke, T. D. (1985). Lateral force displacement response of buried pipe. *J. Geotech. Engng* **111**, No. 9, 1077–92.

White, D. J., Take, W. A. & Bolton, M. D. (2003). Soil deformation measurement using particle image velocimetry (PIV) and photogrammetry. *Géotechnique* **53**, No. 7, 619–631, http://dx.doi.org/10.1680/geot.2003.53.7.619.

White, R. J., Stone, K. J. L. & Jewell, J. J. (1994). Effect of particle size on localisation development in model tests on sand. *Proc. Int. Conf. Centrifuge 94, Singapore*, 817–822.

Yilmaz, M. T. & Paolucci, R. (2007). Earthquake fault rupture–shallow foundation interaction in undrained soils. *Earthquake Engng Struct. Dynam.* **36**, No. 1, 101–118.

Youd, T. L., Bardet, J. P. & Bray, J. D. (2000). Kocaeli, Turkey, earthquake of August 17, 1999: reconnaissance report. *Earthquake Spectra* **16**, Suppl. A, 1–461.